

Salt and pepper noise removal method based on stationary Framelet transform with non-convex sparsity regularization

Yingpin Chen^{1,2}, Lingzhi Wang², Huiying Huang², Jianhua Song², Chaoqun Yu², Yanping Xu²
(1 School of Mathematical Sciences, University of Electronic Science and Technology, 610054;
2 School of Physics and Information Engineering, Minnan Normal University, 363000)

Abstract: Salt and pepper noise removal is a common inverse problem in image processing, and it aims to restore image information with high quality. Traditional salt and pepper denoising methods have two limitations. First, noise characteristics are often not described accurately. For example, the noise location information is often ignored and the sparsity of the salt and pepper noise is often described by l_1 norm, which cannot illustrate the sparse variables clearly. Second, conventional methods separate the contaminated image into a recovered image and a noise part, thus resulting in recovering an image with unsatisfied smooth parts and detail parts. In this study, we introduce a noise detection strategy to determine the position of the noise, and a non-convex sparsity regularization depicted by l_p quasi-norm is employed to describe the sparsity of the noise, thereby addressing the first limitation. The morphological component analysis framework with stationary Framelet transform is adopted to decompose the processed image into cartoon, texture, and noise parts to resolve the second limitation. In this framework, the stationary Framelet regularizations with different parameters control the restoration of the cartoon and texture parts. In this way, the two parts are recovered separately to avoid mutual interference. Then, the alternating direction method of multipliers (ADMM) is employed to solve the proposed model. Finally, experiments are conducted to verify the proposed method and compare it with some current state-of-the-art denoising methods. The experimental results show that the proposed method can remove salt and pepper noise while preserving the details of the processed image.

Keywords: Morphological component analysis, l_p quasi-norm, stationary Framelet transform, ADMM

1. Introduction

Salt and pepper noise is a common interference in contaminated images, and it occurs during image acquisition, transmission, and decoding processes [1]. Salt noise is an impulse value that pollutes the pixel, and pepper noise is a pixel contamination by a zero value [2]. Salt noise may be caused by the random impulse interference. By contrast, pepper noise is mainly caused by a dysfunction of the image acquisition sensor. Salt and pepper noise would cause information missing, resulting in interference of image analyses, such as object segmentation and object recognition. Therefore, salt and pepper denoising is essential in image processing. Fundamentally, the denoising process is an inverse problem that aims to obtain a reconstructed image from a polluted image[3-5].

Common methods for removing salt and pepper noise include median filter-based methods [6-11], total variation (TV) based methods [12-17], deep learning-based methods [18-26], and wavelet transform (WT) based methods [27-30]. Median filter-based methods replace the noise pixel with the median value of adjacent pixels. These methods may distort the image structure and smoothness of the image cohesion. Total variation has been widely used in image denoising. Although total variation-based methods can preserve the edges of the processed image, they easily produce stair-case artifacts when processing the image smoothing area. With the development of deep learning theory, various deep learning-based models have been proposed for image denoising. However, these methods [18-23] require large amounts of sample data and high computational costs for training. WT-based methods [27-30] regard the image as a sparse representation of the wavelet dictionary. As salt and pepper noise occurs randomly, it cannot be

sparingly represented by the wavelet. Thus, WT-based methods are capable of reconstructing the image via wavelet dictionary and removing the salt and pepper noise. Nevertheless, the down-sampling operation of the WT may cause block artifacts in the recovery signal. Additionally, WT only has one high-pass filter, which cannot accurately depict the detail of the processed signal. Scholars have made great efforts to improve the performance of WT. For instance, Wang et al. [31] proposed a non-down-sampling stationary WT to solve the block artifacts in the WT. Yan et al. [32] applied the Framelet transform (FT) [33, 34] to image denoising. Compared with the WT, the FT adds a high-pass filter analysis, which better depicts signal details.

The aforementioned methods have two limitations. On the one hand, conventional methods do not fully explore the characteristics of salt and pepper noise. For example, the location information of salt and pepper noise is often ignored in traditional methods. Additionally, it is easy to detect the location of noise because the amplitude characteristic of noise is peculiar. Furthermore, the sparsity of salt and pepper noise has not been fully explored. In the conventional denoising model, the l_0 norm and l_1 norm are often employed to express the sparsity of sparse variables. The l_0 norm is an ideal tool for depicting sparse variables. However, l_0 norm-based denoising methods are nondeterministic polynomial hard problems. The l_1 norm is the convex relaxation of the l_0 norm. Nonetheless, the capacity of the l_1 norm to depict sparse variables is limited. Recently, the non-convex sparsity regularization depicted by l_p quasi-norm has been widely studied because of its excellent sparsity depiction ability [12, 13, 15, 35-41]. Wang adopted the l_p quasi-norm to depict the sparsity of impulse noise and proposed a denoising method based on low-order overlapping group sparsity with l_p quasi-norm and achieved promising denoising performance [15]. On the other hand, the methods mentioned regard the contaminated image as the sum of the reconstructed image and noise. These methods do not further refine the reconstructed image into low-and high-frequency components. Thus, it is easy to blur the high-frequency components when restoring the low-frequency components of the image. By contrast, it is difficult to remove noise when restoring the high-frequency components of the image. To solve this limitation, researchers introduced the morphological component analysis (MCA) framework [42-46] for image processing. In this framework, the processed image is understood as cartoon, texture, and noise parts. In this way, the cartoon part containing the low-frequency components and the texture part containing the high-frequency components can be reconstructed independently using different regularization parameters. For instance, Chen et al. proposed an MCA-based image deblurring method [47]. Chen et al. adopted the l_0 norm in the data fidelity term in the MCA framework to remove impulse noise in the image [48]. Although, the MCA framework has achieved great success in noise removal, there are still enough room for improvements. Firstly, the sparse transforms used in MCA framework may be unable to express the processed image accurately. For example, the discrete cosine transform used in [47] only achieves sparse coefficients when the processed data is a periodic signal. However, the natural images in the real world rarely fit the condition. The wavelet transform is also often used in MCA framework. However, the implementation of wavelet transform involves a down-sampling operation, resulting in data missing problem in the sparse representation. Secondly, the sparse variables are often expressed by the l_0 norm or l_1 norm. Since the l_0 norm-based problem is a non-deterministic polynomial problem, the l_0 norm induced result is only an approximate solution. Since the l_1 norm is the convex relaxation of l_0 norm, the l_1 norm induced solution may not be the best one. Inspired by the work mentioned above, the stationary Framelet transform (SFT) is adopted as the sparse transform of MCA to further improve the quality of sparse representation for the SFT avoids the down-sampling operator and can represent the image sparsely. In addition, the l_p quasi-norm is adopted in MCA to

improve the capacity of describing the sparse variables like the salt and pepper noise and the coefficients of SFT. Thus, an image denoising model based on MCA with l_p quasi-norm (SFT_Lp) is presented. Considering that the amplitudes of salt and pepper noise are only zero or 255, it is easy to detect the amplitude of the contaminated image to find the location of noise. After detection, the noise location information is modeled as a mask matrix, which is then employed in the proposed MCA-based denoising model to further protect the clean area of the observed image and explore the location information of the noise. Then, the alternating direction method of multipliers (ADMM) [49, 50] is adopted to solve the proposed model. Finally, we conducted experiments on several standard test images and compared them with some denoising methods. The peak signal-to-noise ratio (PSNR) [30], structural similarity index (SSIM) [51], and gradient magnitude similarity deviation (GMSD) [37] were used to evaluate the algorithms. The experimental results showed that the proposed method outperformed the other methods. The contributions of this study are as follows:

(1) The proposed method first determines the noise location, then explores the noise location information and the sparse statistical characteristics of the salt and pepper noise to remove the noise. In this way, the noise cannot interfere with the part without noise pollution during the denoising process.

(2) Compared with current MCA framework, the SFT is adopted instead of WT to avoid block artifacts of the wavelet transform and better represent the natural images.

(3) The l_p quasi-norm is employed to better describe the sparsity of salt and pepper noise and the coefficients of the SFT. Compared with the l_1 norm, the l_p quasi-norm has more freedom, reducing sparser solutions.

(4) The proposed model is successfully solved by ADMM, in which, the proposed model is changed as several decoupled sub-problems to solve.

The rest of this paper is organized as follows. In section 2, the preliminaries of related work are provided for further discussion. In section 3, the proposed model and the ADMM-based solver are provided in detail. In section 4, we show the experiments compared with some state-of-the-art methods and provide the performance of the key components in the proposed method to verify the effective of the proposed method. Finally, we discuss the main conclusions by the experimental results.

2. Preliminaries

In this section, we firstly review the l_p quasi-norm to illustrate the strong capacity of depicting the sparse variables. Then, we provide the preliminaries of two-dimensional SFT to discuss the advantages of SFT. After the introduction of the two signal representation tools, we then discuss the motivation of the proposed method.

2.1 Non-convex sparsity regularization depicted by l_p quasi-norm

The l_p quasi-norm is defined as $\|\mathbf{A}\|_p^p = \sum_{i=1}^N \sum_{j=1}^N |\mathbf{A}_{ij}|^p, p \in (0, 1)$ [15, 16, 37-39, 52]. Figure 1 shows the contours of the l_2 norm, l_1 norm, and l_p quasi-norm. As shown in Figure 1, the contour of the l_p quasi-norm is closer to the axis of the coordinates, reducing a sparser solution than that of the l_2 and l_1 norms. Thus, the advantages of the l_p quasi-norm are as follows: 1) the capacity of a sparse description is intense, and 2) the l_p quasi-norm has more freedoms than the l_1 and l_2 norms for one can select any $p \in (0, 1)$ to fit the degree of sparsity of a sparse variable.

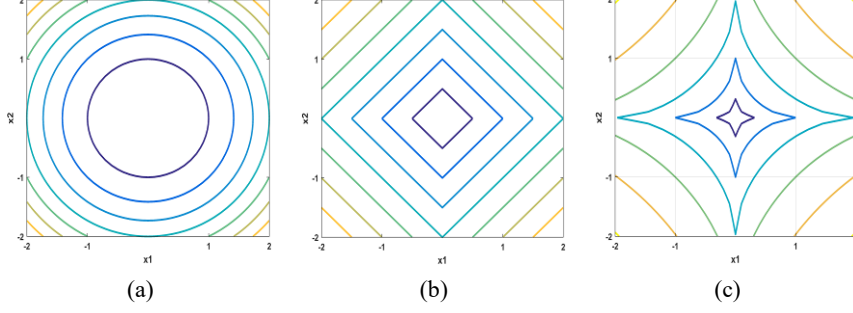


Figure 1 Contours of various norms. (a) l_2 norm; (b) l_1 norm; (c) l_p quasi-norm.

Considering these advantages, we adopt the l_p quasi-norm in the data fidelity term of the MCA framework to express the statistical characteristics of salt and pepper noise. Because the freedom of the l_p quasi-norm lies on the parameter p , it seems easy to control the sparsity of the noise variable when the noise level changes. When the noise pollution level is high, the noise variable may not be highly sparse. In this case, we set the parameter p to a value close to 1. Conversely, when the noise pollution level is low, the noise variable is sparser than in the former case. Thus, the parameter p can be set to a small value close to 0. As discussed above, the l_p quasi-norm can fit the noise level, which helps to adjust the denoising performance in the noise removal process.

2.2 Two-dimensional stationary Framelet transform

The SFT is a combination of stationary and Framelet transform (FT), incorporating the advantages of stationary transform [53] and FT [54]. The SFT is an FT without a down-sampling operation. Thus, the SFT coefficients are the same as those of the original signal. These redundant coefficients ensure the time-invariant property and avoid missing information in the abrupt region of the processed signal. Thus, the recovery signal via the inverse SFT is free from the block artifacts of the traditional wavelet transform. In addition, the FT has one scaling function and two wavelet functions, whereas the WT has only one scaling function and one wavelet function. Therefore, the FT can explore more information than the WT.

Figure 2 shows a schematic sketch of the two-dimensional SFT. In Figure 2(a), the input image \mathbf{F}

is convoluted by three analytical filters: $\tilde{\mathbf{h}}_0 = \left[\frac{1}{4}, \frac{1}{2}, \frac{1}{4} \right]^T$, $\tilde{\mathbf{h}}_1 = \left[\frac{\sqrt{2}}{4}, 0, -\frac{\sqrt{2}}{4} \right]^T$, and $\tilde{\mathbf{h}}_2 = \left[-\frac{1}{4}, \frac{1}{2}, -\frac{1}{4} \right]^T$,

where $\tilde{\mathbf{h}}_0$ is a low-pass filter, and $\tilde{\mathbf{h}}_1$ and $\tilde{\mathbf{h}}_2$ are high-pass filters. Then, the three convolution results

are convoluted by $\tilde{\mathbf{h}}_0^T$, $\tilde{\mathbf{h}}_1^T$, and $\tilde{\mathbf{h}}_2^T$. The final convolution results, \mathbf{F}_{LL} , \mathbf{F}_{H_1L} , \mathbf{F}_{H_2L} , \mathbf{F}_{LH_1} , $\mathbf{F}_{H_1H_1}$,

$\mathbf{F}_{H_2H_1}$, \mathbf{F}_{LH_2} , $\mathbf{F}_{H_1H_2}$, and $\mathbf{F}_{H_2H_2}$ are the results of the SFT. Figure 2(b) shows the inverse SFT. $\hat{\mathbf{F}}$ represents the reconstructed image by inverse SFT, which is the merge-sum of SFT results convoluted

with $\mathbf{h}_0^T = \left[\frac{1}{4}, \frac{1}{2}, \frac{1}{4} \right]$, $\mathbf{h}_1^T = \left[-\frac{\sqrt{2}}{4}, 0, \frac{\sqrt{2}}{4} \right]$, $\mathbf{h}_2^T = \left[-\frac{1}{4}, \frac{1}{2}, -\frac{1}{4} \right]$, $\mathbf{h}_0 = \left[\frac{1}{4}, \frac{1}{2}, \frac{1}{4} \right]^T$, $\mathbf{h}_1 = \left[-\frac{\sqrt{2}}{4}, 0, \frac{\sqrt{2}}{4} \right]^T$,

and $\mathbf{h}_2 = \left[-\frac{1}{4}, \frac{1}{2}, -\frac{1}{4} \right]^T$.

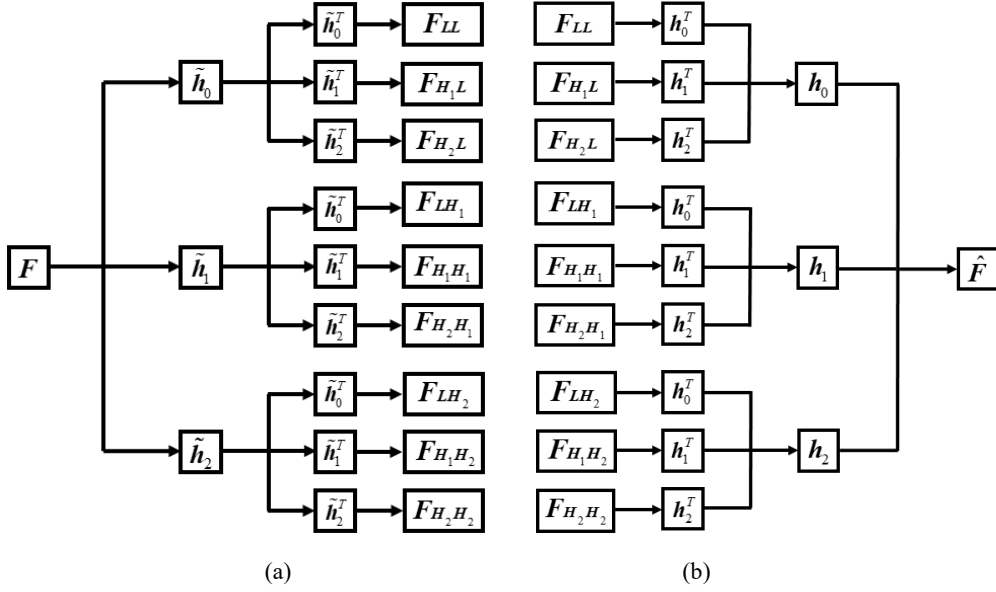


Figure 2 Two-dimensional stationary Framelet transform and inverse transform. (a) Two-dimensional stationary Framelet transform; (b) Two-dimensional inverse SFT.

Since SFT can sparsely represent the natural images without data missing problem in WT, it is more suitable to use the SFT in MCA. By cooperation with the l_p quasi-norm, the noise sparsity and the SFT coefficients can be properly depicted, thus achieving a better reconstructed image.

3. Method

In this section, we first discuss the advantages of MCA framework, then provide the improving MCA-based model in this study. After that, the ADMM is employed to find the solution of the proposed model. Thus, the proposed model is changed as several simple sub-problems, which can be easily calculated.

3.1 Proposed denoising model via morphological component analysis with l_p quasi-norm

MCA [43-46] decomposes the processed image into cartoon and texture parts by sparse representation, where the cartoon part contains the low-frequency components of the image, and the texture part contains the high-frequency components of the image. In this way, the outline and details of the image can be recovered independently. Figure 3 illustrates the principle of MCA, where D denotes the two-dimensional SFT shown in Figure 2; N refers to the noise part; The F_C and F_T represent the cartoon and texture parts, respectively. To fully explore the location information of the noise, we determine the position of the noise via the special amplitude value of salt and pepper noise.

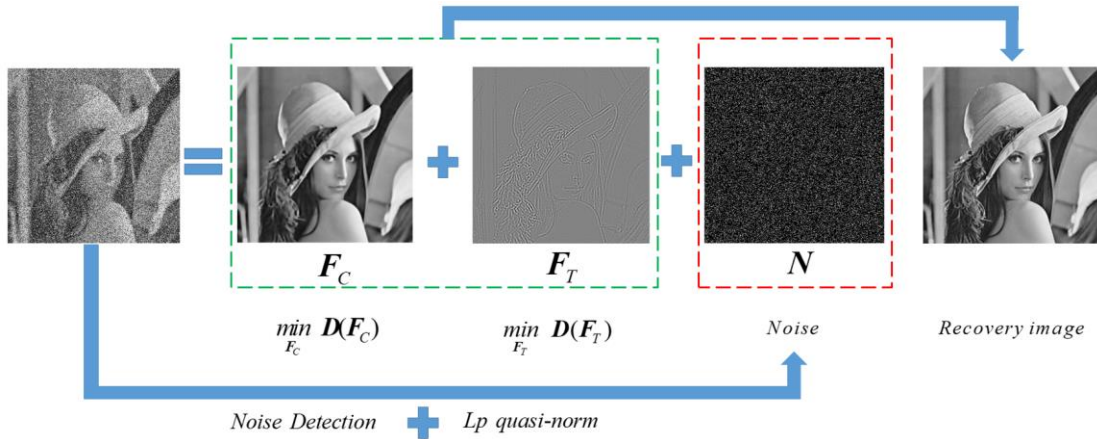


Figure 3 Diagrammatic sketch of the proposed model

Figure 3 illustrates the main idea of the proposed denoising model. In the proposed model, the processed image is considered as the sum of the cartoon, texture, and noise components. The cartoon and texture components are reconstructed separately by using the SFT in the MCA framework. For the special amplitude of the salt and pepper noise, it seems easily to detect the noise location by using the amplitude information. Thus, a noise detection operation is adopted to determine the position of the noise. In addition, the l_p quasi-norm is adopted to depict the statistical characteristics of salt and pepper noise.

As discussed above, we adopt the MCA framework with the non-convex l_p quasi-norm and stationary Framelet transform to further improve the quality of recovery image, the proposed model can be expressed as follows:

$$[\mathbf{F}_T, \mathbf{F}_C] = \underset{[\mathbf{F}_T, \mathbf{F}_C]}{\operatorname{argmin}} \alpha_0 \|\mathbf{M} \circ (\mathbf{F}_T + \mathbf{F}_C) - \mathbf{G}\|_{p_0}^{p_0} + \alpha_1 \|\mathbf{D}(\mathbf{F}_C)\|_{p_1}^{p_1} + \alpha_2 \|\mathbf{D}(\mathbf{F}_T)\|_{p_2}^{p_2}, \quad (1)$$

where \mathbf{G} is the observed image; α_0 is the regularization parameter of the data fidelity $\|\mathbf{M} \circ (\mathbf{F}_T + \mathbf{F}_C) - \mathbf{G}\|_{p_0}^{p_0}$; α_1 and α_2 are the regularization of the sparse prior of \mathbf{F}_C and \mathbf{F}_T ,

respectively; and \mathbf{M} is the mask matrix with the entries $\mathbf{M}(i, j) = \begin{cases} 1, & \text{if } 0 < \mathbf{G}(i, j) < 255 \\ 0, & \text{if } \mathbf{G}(i, j) = 0 \\ 0, & \text{if } \mathbf{G}(i, j) = 255 \end{cases}$; \mathbf{D} refers to

a two-dimensional SFT operator; p_0 , p_1 , and p_2 are the parameters of the l_p quasi-norm, respectively. p_0 is used to describe the sparsity of salt and pepper noise. p_1 and p_2 are adopted to express the sparsity of the FT coefficients of \mathbf{F}_C and \mathbf{F}_T , respectively.

Because \mathbf{F}_C and \mathbf{F}_T are reconstructed independently, they do not interfere with each other during the recovery process. In this way, the final recovery image $\mathbf{F}_C + \mathbf{F}_T$ is capable of preserving the image detail and drastically removing the salt and pepper noise.

3.2 Solver for the proposed model

To solve the proposed model, the ADMM is adopted, where $\mathbf{Q}_0 = \mathbf{M} \circ (\mathbf{F}_T + \mathbf{F}_C) - \mathbf{G}$, $\mathbf{Q}_1 = \mathbf{D}(\mathbf{F}_C)$, and $\mathbf{Q}_2 = \mathbf{D}(\mathbf{F}_T)$. Introduce the dual variables $\tilde{\mathbf{Q}}_0$, $\tilde{\mathbf{Q}}_1$, and $\tilde{\mathbf{Q}}_2$ with regard to \mathbf{Q}_0 , \mathbf{Q}_1 , and \mathbf{Q}_2 ; the augmented Lagrange function of the proposed model is as follows:

$$\begin{aligned} \mathbf{J} = \max_{\tilde{\mathbf{Q}}_0, \tilde{\mathbf{Q}}_1, \tilde{\mathbf{Q}}_2} \{ \min_{\mathbf{F}_C, \mathbf{F}_T, \mathbf{Q}_0, \mathbf{Q}_1, \mathbf{Q}_2} \{ & \alpha_0 \|\mathbf{Q}_0\|_{p_0}^{p_0} + \alpha_1 \|\mathbf{Q}_1\|_{p_1}^{p_1} + \alpha_2 \|\mathbf{Q}_2\|_{p_2}^{p_2} - \langle \lambda_0 \tilde{\mathbf{Q}}_0, \mathbf{Q}_0 - [\mathbf{M} \circ (\mathbf{F}_T + \mathbf{F}_C) - \mathbf{G}] \rangle \\ & + \frac{\lambda_0}{2} \|\mathbf{Q}_0 - [\mathbf{M} \circ (\mathbf{F}_T + \mathbf{F}_C) - \mathbf{G}]\|_2^2 - \langle \lambda_1 \tilde{\mathbf{Q}}_1, \mathbf{Q}_1 - \mathbf{D}(\mathbf{F}_C) \rangle + \frac{\lambda_1}{2} \|\mathbf{Q}_1 - \mathbf{D}(\mathbf{F}_C)\|_2^2 \\ & - \langle \lambda_2 \tilde{\mathbf{Q}}_2, \mathbf{Q}_2 - \mathbf{D}(\mathbf{F}_T) \rangle + \frac{\lambda_2}{2} \|\mathbf{Q}_2 - \mathbf{D}(\mathbf{F}_T)\|_2^2 \} \}, \end{aligned} \quad (2)$$

where λ_0 , λ_1 , and λ_2 represent coefficients of quadratic penalty term $\|\mathbf{Q}_0 - [\mathbf{M} \circ (\mathbf{F}_T + \mathbf{F}_C) - \mathbf{G}]\|_2^2$, $\|\mathbf{Q}_1 - \mathbf{D}(\mathbf{F}_C)\|_2^2$, and $\|\mathbf{Q}_2 - \mathbf{D}(\mathbf{F}_T)\|_2^2$.

To find the solution of (2), we solve the following subproblems with regard to each variable separately.

(1) \mathbf{F}_C sub-problem

The corresponding objective function of \mathbf{F}_C is as follows:

$$\begin{aligned} J_{F_C} = \min_{F_C} \{ & -\langle \lambda_0 \tilde{\mathbf{Q}}_0^{(k)}, \mathbf{Q}_0^{(k)} - [\mathbf{M} \circ (\mathbf{F}_T^{(k)} + \mathbf{F}_C) - \mathbf{G}] \rangle + \frac{\lambda_0}{2} \|\mathbf{Q}_0^{(k)} - [\mathbf{M} \circ (\mathbf{F}_T^{(k)} + \mathbf{F}_C) - \mathbf{G}]\|_2^2 \\ & - \langle \lambda_1 \tilde{\mathbf{Q}}_1^{(k)}, \mathbf{Q}_1^{(k)} - \mathbf{D}(\mathbf{F}_C) \rangle + \frac{\lambda_1}{2} \|\mathbf{Q}_1^{(k)} - \mathbf{D}(\mathbf{F}_C)\|_2^2 \}. \end{aligned} \quad (3)$$

By using the method of completing the square, equation (3) becomes

$$F_C = \operatorname{argmin}_{F_C} \left\{ \frac{\lambda_0}{2} \|\mathbf{Q}_0^{(k)} - [\mathbf{M} \circ (\mathbf{F}_T^{(k)} + \mathbf{F}_C) - \mathbf{G}] - \tilde{\mathbf{Q}}_0^{(k)}\|_2^2 + \frac{\lambda_1}{2} \|\mathbf{Q}_1^{(k)} - \mathbf{D}(\mathbf{F}_C) - \tilde{\mathbf{Q}}_1^{(k)}\|_2^2 \right\}. \quad (4)$$

Let $\frac{\partial J_{F_C}}{\partial F_C} = \mathbf{0}$, we have

$$\lambda_0 \mathbf{M} \circ \{ [\mathbf{M} \circ (\mathbf{F}_T^{(k)} + \mathbf{F}_C) - \mathbf{G}] + \tilde{\mathbf{Q}}_0^{(k)} - \mathbf{Q}_0^{(k)} \} + \lambda_1 \mathbf{D}^T (\mathbf{D}(\mathbf{F}_C) + \tilde{\mathbf{Q}}_1^{(k)} - \mathbf{Q}_1^{(k)}) = \mathbf{0}, \quad (5)$$

where \mathbf{D}^T represents the inverse SFT operator.

Organize equation (5) as follows:

$$\lambda_0 \mathbf{M} \circ \mathbf{M} \circ \mathbf{F}_C + \lambda_1 \mathbf{F}_C = \lambda_0 \mathbf{M} \circ \mathbf{G} + \lambda_0 \mathbf{M} \circ (\mathbf{Q}_0^{(k)} - \tilde{\mathbf{Q}}_0^{(k)}) + \lambda_1 \mathbf{D}^T (\mathbf{Q}_1^{(k)} - \tilde{\mathbf{Q}}_1^{(k)}) - \lambda_0 \mathbf{M} \circ \mathbf{M} \circ \mathbf{F}_T^{(k)}. \quad (6)$$

As $\mathbf{M} \circ \mathbf{M} \circ \mathbf{F}_C = \mathbf{M} \circ \mathbf{F}_C$, we have

$$\lambda_0 \mathbf{M} \circ \mathbf{F}_C + \lambda_1 \mathbf{F}_C = \lambda_0 \mathbf{M} \circ \mathbf{G} + \lambda_0 \mathbf{M} \circ (\mathbf{Q}_0^{(k)} - \tilde{\mathbf{Q}}_0^{(k)}) + \lambda_1 \mathbf{D}^T (\mathbf{Q}_1^{(k)} - \tilde{\mathbf{Q}}_1^{(k)}) - \lambda_0 \mathbf{M} \circ \mathbf{F}_T^{(k)}. \quad (7)$$

Let $\mathbf{x} = \mathbf{F}_C$, $\mathbf{A}(\mathbf{x}) = \lambda_0 \mathbf{M} \circ \mathbf{x} + \lambda_1 \mathbf{x}$, and

$\mathbf{b} = \lambda_0 \mathbf{M} \circ \mathbf{G} + \lambda_0 \mathbf{M} \circ (\mathbf{Q}_0^{(k)} - \tilde{\mathbf{Q}}_0^{(k)}) + \lambda_1 \mathbf{D}^T (\mathbf{Q}_1^{(k)} - \tilde{\mathbf{Q}}_1^{(k)}) - \lambda_0 \mathbf{M} \circ \mathbf{F}_T^{(k)}$; then, equation (7) becomes $\mathbf{A}(\mathbf{x}) = \mathbf{b}$.

The conjugate gradient method (CGM) [55] can be used to solve this problem. The CGM is presented in Algorithm 1.

Algorithm 1: Algorithm of CGM

Input: the operator $\mathbf{A}(\mathbf{x})$, the righthand term \mathbf{b} , the maximum number of iterations K .

Output: the resolution \mathbf{x} .

Initialize: the initial solution $\mathbf{x}^{(0)} = \mathbf{0}$, $\mathbf{p}^{(0)} = \mathbf{r}^{(0)}$.

1: Compute the residual $\mathbf{r}^{(0)} = \mathbf{b} - \mathbf{A}\mathbf{x}^{(0)}$;

2: **For** $k = 0, 1, \dots, K$ **do**

3: **If** $\mathbf{p}^{(k)} = \mathbf{0}$

4: **Return** $\mathbf{x}^{(0)}$.

5: **Else**

6: $\mathbf{a}^{(k)} = \frac{(\mathbf{r}^{(k)})^T \mathbf{r}^{(k)}}{(\mathbf{p}^{(k)})^T \mathbf{A}(\mathbf{p}^{(k)})}$;

7: $\mathbf{x}^{(k+1)} = \mathbf{x}^{(k)} + \mathbf{a}^{(k)} \mathbf{p}^{(k)}$;

8: $\mathbf{r}^{(k+1)} = \mathbf{r}^{(k)} - \mathbf{a}^{(k)} \mathbf{A}(\mathbf{p}^{(k)})$;

9: $\mathbf{c}^{(k)} = \frac{(\mathbf{r}^{(k+1)})^T \mathbf{r}^{(k+1)}}{(\mathbf{r}^{(k)})^T \mathbf{r}^{(k)}}$;

10: $\mathbf{p}^{(k+1)} = \mathbf{r}^{(k+1)} + \mathbf{c}^{(k)} \mathbf{p}^{(k)}$;

11: **End**

$$12: \quad \mathbf{If} \quad \frac{\|\mathbf{x}^{(k+1)} - \mathbf{x}^{(k)}\|_2}{\|\mathbf{x}^{(k)}\|_2} < tol$$

13: break;

14: **End**

15: **End**

16: **Return** $\mathbf{x}^{(k+1)}$.

$tol=10^{-4}$ denotes the iterative threshold of the CGM algorithm.

(2) \mathbf{F}_T sub-problem

The corresponding objective function of \mathbf{F}_T is as follows:

$$J_{F_T} = \min_{F_T} \{ -\langle \lambda_0 \tilde{\mathbf{Q}}_0^{(k)}, \mathbf{Q}_0^{(k)} - [\mathbf{M} \circ (\mathbf{F}_T + \mathbf{F}_C^{(k+1)}) - \mathbf{G}] \rangle + \frac{\lambda_0}{2} \|\mathbf{Q}_0^{(k)} - [\mathbf{M} \circ (\mathbf{F}_T + \mathbf{F}_C) - \mathbf{G}]\|_2^2 - \langle \lambda_2 \tilde{\mathbf{Q}}_2^{(k)}, \mathbf{Q}_2^{(k)} - \mathbf{D}(\mathbf{F}_T) \rangle + \frac{\lambda_2}{2} \|\mathbf{Q}_2^{(k)} - \mathbf{D}(\mathbf{F}_T)\|_2^2 \}. \quad (8)$$

By using the method of completing the square, equation (8) becomes

$$J_{F_T} = \min_{F_T} \left\{ \frac{\lambda_0}{2} \|\mathbf{Q}_0 - [\mathbf{M} \circ (\mathbf{F}_T + \mathbf{F}_C) - \mathbf{G}] - \tilde{\mathbf{Q}}_0\|_2^2 + \frac{\lambda_2}{2} \|\mathbf{Q}_2 - \mathbf{D}(\mathbf{F}_T) - \tilde{\mathbf{Q}}_2\|_2^2 \right\}. \quad (9)$$

Let $\frac{\partial J_{F_T}}{\partial \mathbf{F}_T} = \mathbf{0}$, then we have

$$\lambda_0 \mathbf{M} \circ \mathbf{F}_T^{(k+1)} + \lambda_2 \mathbf{F}_T^{(k+1)} = \lambda_0 \mathbf{M} \circ \mathbf{G} + \lambda_0 \mathbf{M} \circ (\mathbf{Q}_0^{(k)} - \tilde{\mathbf{Q}}_0^{(k)}) + \lambda_2 \mathbf{D}^T(\mathbf{Q}_2^{(k)} - \tilde{\mathbf{Q}}_2^{(k)}) - \lambda_0 \mathbf{M} \circ \mathbf{F}_C^{(k+1)}. \quad (10)$$

Let $\mathbf{x} = \mathbf{F}_T$, $\mathbf{A}(\mathbf{x}) = \lambda_0 \mathbf{M} \circ \mathbf{x} + \lambda_2 \mathbf{x}$,

$\mathbf{b} = \lambda_0 \mathbf{M} \circ \mathbf{G} + \lambda_0 \mathbf{M} \circ (\mathbf{Q}_0^{(k)} - \tilde{\mathbf{Q}}_0^{(k)}) + \lambda_2 \mathbf{D}^T(\mathbf{Q}_2^{(k)} - \tilde{\mathbf{Q}}_2^{(k)}) - \lambda_0 \mathbf{M} \circ \mathbf{F}_C^{(k+1)}$; then calculate \mathbf{F}_T in (10) using the CGM algorithm.

(3) \mathbf{Q}_0 sub-problem

The \mathbf{Q}_0 sub-problem is as follows:

$$J_{Q_0} = \min_{Q_0} \{ \alpha_0 \|\mathbf{Q}_0\|_{p_0}^{p_0} - \langle \lambda_0 \tilde{\mathbf{Q}}_0^{(k)}, \mathbf{Q}_0 - [\mathbf{M} \circ (\mathbf{F}_T^{(k+1)} + \mathbf{F}_C^{(k+1)}) - \mathbf{G}] \rangle + \frac{\lambda_0}{2} \|\mathbf{Q}_0 - [\mathbf{M} \circ (\mathbf{F}_T^{(k+1)} + \mathbf{F}_C^{(k+1)}) - \mathbf{G}]\|_2^2 \}. \quad (11)$$

By using the method of completing the square, equation (11) becomes

$$\mathbf{Q}_0 = \underset{Q_0}{\operatorname{argmin}} \left\{ \alpha_0 \|\mathbf{Q}_0\|_{p_0}^{p_0} + \frac{\lambda_0}{2} \|\mathbf{Q}_0 - [\mathbf{M} \circ (\mathbf{F}_T^{(k+1)} + \mathbf{F}_C^{(k+1)}) - \mathbf{G}] - \tilde{\mathbf{Q}}_0\|_2^2 \right\}. \quad (12)$$

The solution of equation (12) can be found by l_p shrinkage [41], that is,

$$\mathbf{Q}_0^{(k+1)} = \max \left\{ \left| \Theta_0 \right| - \left(\frac{\lambda_0}{\alpha_0} \right)^{p_0-2} \left| \Theta_0 \right|^{p_0-1}, 0 \right\} \frac{\Theta_0}{\left| \Theta_0 \right|}, \quad (13)$$

where $\Theta_0 = \mathbf{M} \circ (\mathbf{F}_T^{(k+1)} + \mathbf{F}_C^{(k+1)}) - \mathbf{G} + \tilde{\mathbf{Q}}_0^{(k)}$.

(4) \mathbf{Q}_1 sub-problem

The \mathbf{Q}_1 sub-problem is as follows:

$$J_{Q_1} = \min_{Q_1} \left\{ \alpha_1 \|\mathbf{Q}_1\|_{p_1}^{p_1} - \langle \lambda_1 \tilde{\mathbf{Q}}_1^{(k)}, \mathbf{Q}_1 - \mathbf{D}(\mathbf{F}_C^{(k+1)}) \rangle + \frac{\lambda_1}{2} \|\mathbf{Q}_1 - \mathbf{D}(\mathbf{F}_C^{(k+1)})\|_2^2 \right\}. \quad (14)$$

By using the method of completing the square, equation (14) becomes

$$\mathbf{Q}_1 = \underset{\mathbf{Q}_1}{\operatorname{argmin}} \left\{ \alpha_1 \|\mathbf{Q}_1\|_{p_1}^{p_1} + \frac{\lambda_1}{2} \|\mathbf{Q}_1 - \mathbf{D}(\mathbf{F}_C^{(k+1)}) - \tilde{\mathbf{Q}}_1^{(k)}\|_2^2 \right\}. \quad (15)$$

By using the l_p shrinkage, we have

$$\mathbf{Q}_1^{(k+1)} = \operatorname{shrink}_{p_1} \left(\Theta_1, \frac{\alpha_1}{\lambda_1} \right) = \max \left\{ |\Theta_1| - \left(\frac{\lambda_1}{\alpha_1} \right)^{p_1-2} |\Theta_1|^{p_1-1}, 0 \right\} \frac{\Theta_1}{|\Theta_1|}, \quad (16)$$

where $\Theta_1 = \mathbf{D}(\mathbf{F}_C^{(k+1)}) + \tilde{\mathbf{Q}}_1^{(k)}$.

(5) \mathbf{Q}_2 sub-problem

The \mathbf{Q}_2 sub-problem is as follows:

$$J_{\mathbf{Q}_2} = \alpha_2 \|\mathbf{Q}_2\|_{p_2}^{p_2} - \langle \lambda_2 \tilde{\mathbf{Q}}_2^{(k)}, \mathbf{Q}_2 - \mathbf{D}(\mathbf{F}_T^{(k+1)}) \rangle + \frac{\lambda_2}{2} \|\mathbf{Q}_2 - \mathbf{D}(\mathbf{F}_T^{(k+1)})\|_2^2. \quad (17)$$

By using the method of completing the square, we have

$$\mathbf{Q}_2 = \underset{\mathbf{Q}_2}{\operatorname{argmin}} \left\{ \alpha_2 \|\mathbf{Q}_2\|_{p_2}^{p_2} + \frac{\lambda_2}{2} \|\mathbf{Q}_2 - \mathbf{D}(\mathbf{F}_T^{(k+1)}) - \tilde{\mathbf{Q}}_2^{(k)}\|_2^2 \right\}. \quad (18)$$

By using the l_p shrinkage, we have

$$\mathbf{Q}_2^{(k+1)} = \operatorname{shrink}_{p_2} \left(\Theta_2, \frac{\alpha_2}{\lambda_2} \right) = \max \left\{ |\Theta_2| - \left(\frac{\lambda_2}{\alpha_2} \right)^{p_2-2} |\Theta_2|^{p_2-1}, 0 \right\} \frac{\Theta_2}{|\Theta_2|}, \quad (19)$$

where $\Theta_2 = \mathbf{D}(\mathbf{F}_T^{(k+1)}) + \tilde{\mathbf{Q}}_2^{(k)}$.

(6) $\tilde{\mathbf{Q}}_0$ sub-problem

The $\tilde{\mathbf{Q}}_0$ sub-problem is as follows:

$$J_{\tilde{\mathbf{Q}}_0} = \max_{\tilde{\mathbf{Q}}_0} \left\{ -\langle \lambda_0 \tilde{\mathbf{Q}}_0, \mathbf{Q}_0^{(k+1)} - [\mathbf{M} \circ (\mathbf{F}_T^{(k+1)} + \mathbf{F}_C^{(k+1)}) - \mathbf{G}] \rangle \right\}. \quad (20)$$

By using the gradient ascend method, we have

$$\tilde{\mathbf{Q}}_0^{(k+1)} = \tilde{\mathbf{Q}}_0^{(k)} + \gamma \lambda_0 [\mathbf{M} \circ (\mathbf{F}_T^{(k+1)} + \mathbf{F}_C^{(k+1)}) - \mathbf{G} - \mathbf{Q}_0], \quad (21)$$

where γ represents the learning ratio.

(7) $\tilde{\mathbf{Q}}_1$ sub-problem

The $\tilde{\mathbf{Q}}_1$ sub-problem is as follows:

$$J_{\tilde{\mathbf{Q}}_1} = \max_{\tilde{\mathbf{Q}}_1} \left\{ -\langle \lambda_1 \tilde{\mathbf{Q}}_1, \mathbf{Q}_1^{(k+1)} - \mathbf{D}(\mathbf{F}_C^{(k+1)}) \rangle \right\}. \quad (22)$$

By using the gradient ascend method, we have

$$\tilde{\mathbf{Q}}_1^{(k+1)} = \tilde{\mathbf{Q}}_1^{(k)} + \gamma \lambda_1 [\mathbf{D}(\mathbf{F}_C^{(k+1)}) - \mathbf{Q}_1^{(k+1)}]. \quad (23)$$

(8) $\tilde{\mathbf{Q}}_2$ sub-problem

The $\tilde{\mathbf{Q}}_2$ sub-problem is as follows:

$$J_{\tilde{\mathbf{Q}}_2} = \max_{\tilde{\mathbf{Q}}_2} \left\{ -\langle \lambda_2 \tilde{\mathbf{Q}}_2, \mathbf{Q}_2^{(k+1)} - \mathbf{D}(\mathbf{F}_T^{(k+1)}) \rangle \right\}. \quad (24)$$

By using the gradient ascend method, we have

$$\tilde{\mathbf{Q}}_2^{(k+1)} = \tilde{\mathbf{Q}}_2^{(k)} + \gamma \lambda_2 [\mathbf{D}(\mathbf{F}_T^{(k+1)}) - \mathbf{Q}_2^{(k+1)}]. \quad (25)$$

Algorithm 2: The proposed method

Input: the observed image G .

Output: the recovered image $F = F_C + F_T$.

Initialize: $F_C^{(0)}, F_T^{(0)}, F^{(0)}, Q_0^{(0)}, Q_1^{(0)}, Q_2^{(0)}, \tilde{Q}_0^{(0)}, \tilde{Q}_1^{(0)}, \tilde{Q}_2^{(0)} = \mathbf{0}$, the maximum number of iterations K .

1: **For** $k = 0, 1, \dots, K$ **do**;

2: Compute $F_C^{(k+1)}$ by solving equation (7) via **algorithm 1**;

3: Compute $F_T^{(k+1)}$ by solving equation (10) via **algorithm 1**;

4: $F^{(k+1)} = F_C^{(k+1)} + F_T^{(k+1)}$;

5: Update $Q_0^{(k+1)}$ by equation (13);

6: Update $Q_1^{(k+1)}$ by equation (16);

7: Update $Q_2^{(k+1)}$ by equation (19);

8: Update $\tilde{Q}_0^{(k+1)}$ by equation (21);

9: Update $\tilde{Q}_1^{(k+1)}$ by equation (23);

10: Update $\tilde{Q}_2^{(k+1)}$ by equation (25);

11: **If** $\frac{\|F^{(k+1)} - F^{(k)}\|_2}{\|F^{(k)}\|_2} < tol$;

12: break;

13: **End**

14: **End**

15: **Return** $F^{(k+1)}$.

where the maximal iteration number K is set as 100 and the iteration stop threshold tol is set as 10^{-4} .

4. Experiments

In this section, we provide abundant experiments to verify the proposed method. We firstly provide the main measure indexes used in this paper, then compare the proposed method with some state-of-the-art methods and verify the effectiveness of the key components of the proposed method by using ablation experiments.

4.1 Algorithm evaluation indexes and parameter setting

We adopted some common image evaluation indexes to estimate the quality of the recovered image using different algorithms. The evaluation indexes used in this experiments were the peak signal-to-noise ratio (PSNR) [30], structural similarity index (SSIM) [51], and gradient magnitude similarity deviation (GMSD) [37, 56].

The peak signal-to-noise ratio (PSNR) [30] is the most common and widely used objective measurement of image recovery, and it is computed as follows:

$$PSNR(\mathbf{X}, \mathbf{Y}) = 10 \lg \frac{(\max(\mathbf{X}))^2}{\frac{1}{N^2} \sum_{i=1}^N \sum_{j=1}^N (\mathbf{X}_{ij} - \mathbf{Y}_{ij})^2}, \quad (26)$$

where $\mathbf{X} \in \mathbb{R}^{M \times N}$ represents the original image, and $\mathbf{Y} \in \mathbb{R}^{M \times N}$ represents the recovered image. A high PSNR value indicates that the reconstructed image is highly similar to the original image.

Structural similarity is an objective measurement of image recovery, which is defined as

$$SSIM(\mathbf{X}, \mathbf{Y}) = \frac{(2u_x u_y + (Lk_1)^2)(2\sigma_{xy} + (Lk_2)^2)}{(u_x^2 + u_y^2 + (Lk_1)^2)(\sigma_x^2 + \sigma_y^2 + (Lk_2)^2)}, \quad (27)$$

where u_x is the mean value of X , u_y is the mean value of Y , σ_x^2 is the variance of X , σ_y^2 is the variance of Y , σ_{xy} is the covariance of X and Y , L is the maximum gray value of X , and k_1 and k_2 are the parameters maintaining the denominator as a non-zero number. The SSIM should be within a range of $[0, 1]$. When the reconstructed image is similar to the original image, the SSIM should be close to 1.

The gradient magnitude similarity deviation [37] is another objective measurement of image recovery, which is defined as

$$GMSD = \sqrt{\frac{1}{MN} \sum_{i=1}^M \sum_{j=1}^N \left\{ [GMS]_{i,j} - \frac{1}{MN} \sum_{i=1}^M \sum_{j=1}^N [GMS]_{i,j} \right\}^2}, \quad (28)$$

where $[GMS]_{i,j}$ represents the local gradient magnitude similarity with regard to the pixels in the i -th row and j -th column in the processed image. This is defined as follows:

$$[GMS]_{i,j} = \frac{2[m_x]_{i,j}[m_y]_{i,j} + c}{[m_x]_{i,j}^2 + [m_y]_{i,j}^2 + c}, \quad (29)$$

where c is a constant that keeps the denominator a nonzero number. $[m_x]_{i,j}$ and $[m_y]_{i,j}$ represent the gradient magnitudes of X and Y at the i -th row and j -th column in the processed image, respectively, which are defined as follows:

$$[m_x]_{i,j} = \sqrt{[X * \mathbf{h}_1]_{i,j}^2 + [X * \mathbf{h}_2]_{i,j}^2}, \quad (30)$$

$$[m_y]_{i,j} = \sqrt{[Y * \mathbf{h}_1]_{i,j}^2 + [Y * \mathbf{h}_2]_{i,j}^2}, \quad (31)$$

where the symbol $*$ denotes the convolution operator; \mathbf{h}_1 and \mathbf{h}_2 are defined as follows:

$$\mathbf{h}_1 = \begin{bmatrix} 1/3 & 0 & 1/3 \\ 1/3 & 0 & 1/3 \\ 1/3 & 0 & 1/3 \end{bmatrix}, \mathbf{h}_2 = \begin{bmatrix} 1/3 & 1/3 & 1/3 \\ 0 & 0 & 0 \\ 1/3 & 1/3 & 1/3 \end{bmatrix} \dots \quad (32)$$

When the value of GMSD is small, the deviation of the gradient magnitude similarity between the reconstructed image and the original image is small. Thus, the smaller the GMSD, the higher the quality of the recovered image.

We selected eight standard images, shown in Figure 4, to verify the effectiveness of the proposed

model. To compare the proposed model with other methods efficiently, the images were down-sampled to 256×256 ; only Lena (Figure 4(f)) has two sizes: 512×512 and 256×256 .



Figure 4 Standard test images. (a) Boat; (b) Barbara; (c) Camera; (d) Gold hill; (e) House; (f) Lena; (g) Man; (h) Peppers.

Parameter setting: in the subsequent, the parameters were selected as follows, $p_0, p_1, p_2 \in (0, 1)$, these parameters should be adjusted to achieve the best denoising performance. The parameter p_0 is set to depict the degree of noise sparsity. Typically, when the noise level is low, p_0 should be adjusted near to 0. On the contrary, when the noise level is high, i.e. the noise variable is not sparse enough, p_0 should be adjusted as a number near to 1; The parameter p_1 is set to describe the sparsity of cartoon part in Framelet domain, which should be set larger than p_2 that controls the sparsity of texture part in Framelet domain for we assume that the texture parts are more sparse than the cartoon parts; $\alpha_0=1$; α_1, α_2 were set in the range $[0, 10]$. The parameter α_1 is set to control the sparsity of cartoon parts in Framelet domain and α_2 is set for the sparsity of texture parts in Framelet domain. It is assumed that the texture parts are more sparse than the cartoon parts, thus we set $\alpha_1 = \frac{1}{2} \alpha_2$ for convenience; $\lambda_0, \lambda_1, \lambda_2$ were set in the range $[0, 1]$; $\gamma=1E-6$.

4.2 Comparison with some TV-based methods

In this section, we compared the proposed method (SFT_Lp) with some TV-based methods, which are based on the anisotropic total variation (ATV) [14], isotropic total variation (ITV) [57], isotropic total variation (ITV) with l_p quasi-norm (ITV_Lp), low-order overlapping group sparsity with l_p quasi-norm (LOGS_Lp) [15], and high-order overlapping group sparsity [58] with l_p quasi-norm (HOGS_Lp). The noise levels in this section are 10%, 20%, and 30%, respectively.

Tables 1–3 present the comparison results; the best performances are in bold font. The Lena image of size 512×512 is denoted as “Lena512” in the tables. The remaining images in the tables were down-sampled to 256×256 . It is clear from the tables that the proposed method outperforms the other methods. As seen in the tables, the ITV_Lp denoising model outperforms the ITV denoising model in most cases. In Table 1, for example, the PSNR of the ITV_Lp model is 5.3987 dB higher than that of the ITV model

for Lena512. This is because we used the L_p quasi-norm instead of the l_1 norm in the data fidelity term. This result suggests that the L_p quasi-norm can depict the statistical characteristics of the sparse variable more precisely than the l_1 norm. The ITV_Lp, LOGS_Lp, HOGS_Lp, and the proposed methods all employ the L_p quasi-norm in the data fidelity. Under these conditions, we found that the stationary Framelet regularization in the proposed model outperformed that in the ITV_Lp, LOGS_Lp, and HOGS_Lp models.

To further determine the reconstructed image quality, we used the proposed model as well as the ATV, ITV, ITV_Lp, LOGS_Lp, and HOGS_Lp models to restore the Boat and Lena images for local magnification. The results are shown in Figures 5 and 6. As shown in Figure 5, the recovery image obtained by the proposed model preserves the details of the processed image while total variation-based method may blur the edge of the processed image. As shown in Figure 6, an eye and an eyebrow of Lena were perfectly reconstructed by the proposed model, whereas the compared methods failed to recover these details.

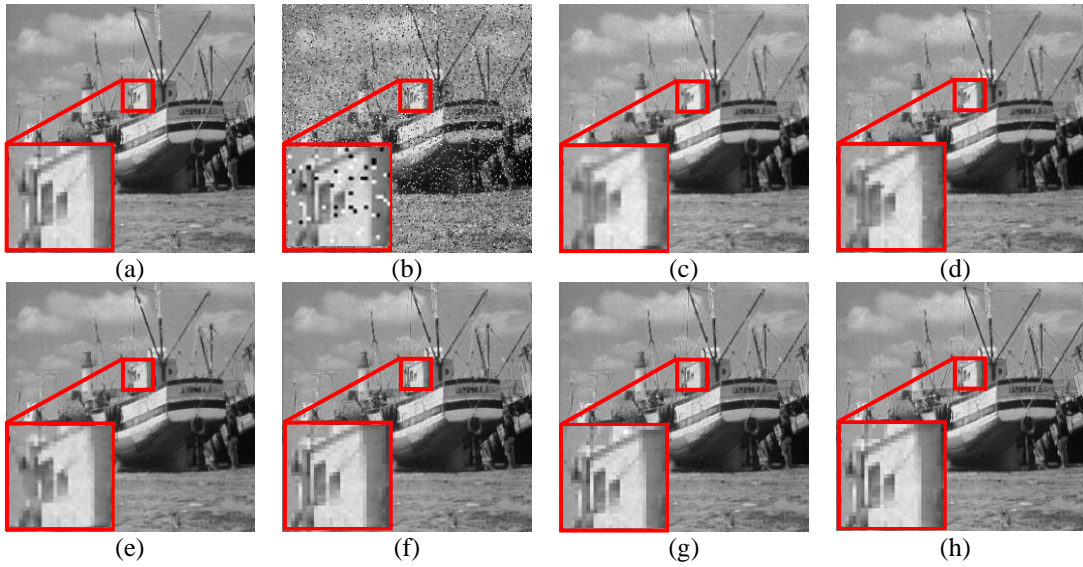


Figure 5 A partial enlarged view of the “Boat” at 10% salt and pepper noise. (a) Original image of “Boat”; (b) “Boat” under 10% noise level interference; (c) ATV method; (d) ITV method; (e) ITV_Lp method; (f) LOGS_Lp method; (g) HOGS_Lp method; (h) proposed method.

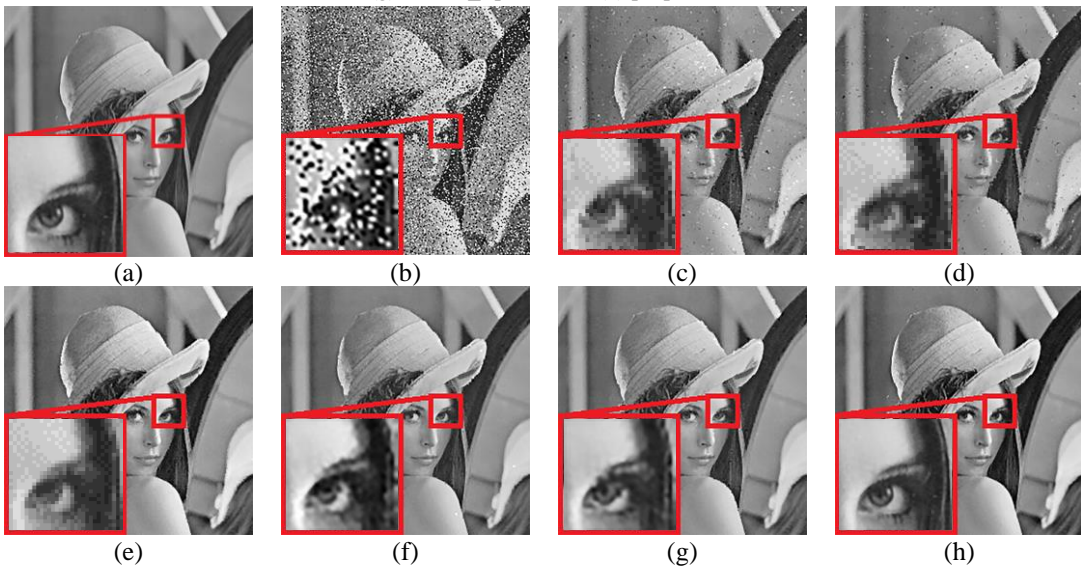


Figure 6 A partial enlarged view of the “Lena512” under 20% salt and pepper noise. (a) Original image of “Lena512”; (b) “Lena512” under 10% noise level interference; (c) ATV method; (d) ITV method; (e) ITV_Lp

method; (f) LOGS_Lp method; (g) HOGS_Lp method; (h) proposed method.

Figure 7 illustrates the dynamic iteration curves for Lena512 using different algorithms under 10% salt and pepper noise. For fair comparison, the stop iteration threshold parameter tol of all the compared methods is set as 10^{-4} . It is clear that the proposed model quickly converges to the final solution and outperforms the compared algorithms.

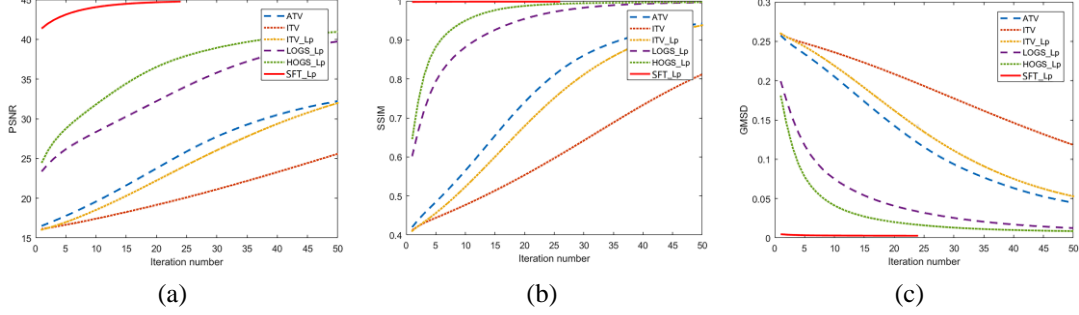


Figure 7 The dynamic iterative diagrams of the PSNR, SSIM, and GMSD values of Lena512 under different noise levels. Dynamic iterative graph of the (a) PSNR value under 10% salt and pepper noise; (b) SSIM value under 10% salt and pepper noise; (c) GMSD value under 10% salt and pepper noise.

Table 1 Performance of the different algorithms under 10% noise level

Processed image		ATV	ITV	ITV_Lp	LOGS_Lp	HOGS_Lp	SFT_Lp
Lena512	PSNR	33.5205	33.8068	39.2055	42.4034	42.6865	45.7682
	SSIM	0.9690	0.9726	0.9951	0.9972	0.9976	0.9983
	GMSD	0.0361	0.0344	0.0105	0.0053	0.0046	0.0022
Lena	PSNR	31.0903	31.9685	32.2948	33.7134	34.1063	39.9352
	SSIM	0.8849	0.9673	0.9599	0.9712	0.9740	0.9886
	GMSD	0.0315	0.0247	0.0301	0.0240	0.0217	0.0062
House	PSNR	36.5603	36.9685	39.3159	41.9909	42.2146	46.8257
	SSIM	0.9573	0.9673	0.9754	0.9897	0.9717	0.9928
	GMSD	0.0202	0.0247	0.0184	0.0103	0.0193	0.0020
Gold hill	PSNR	30.5327	30.6595	31.4325	34.1119	34.3316	37.6899
	SSIM	0.9029	0.9139	0.9417	0.9636	0.9643	0.9794
	GMSD	0.0361	0.0357	0.0429	0.0222	0.0211	0.0084
Man	PSNR	30.1133	30.1821	30.7684	31.5415	31.8264	39.7596
	SSIM	0.8946	0.9113	0.9354	0.9508	0.9545	0.9818
	GMSD	0.0365	0.0380	0.0383	0.0381	0.0363	0.0104
Peppers	PSNR	30.3114	30.5218	30.7067	31.6305	31.8503	40.6575
	SSIM	0.9620	0.9531	0.9602	0.9770	0.9763	0.9890
	GMSD	0.0367	0.0393	0.0342	0.0332	0.0308	0.0043
Camera	PSNR	25.1765	25.2972	25.4175	25.7847	26.2206	38.3257
	SSIM	0.7864	0.8591	0.8675	0.9225	0.9258	0.9903
	GMSD	0.0727	0.0715	0.1093	0.0725	0.0681	0.0087
Barbara	PSNR	25.3605	25.3700	25.7964	25.3605	26.2594	34.7140
	SSIM	0.7804	0.8338	0.8238	0.7804	0.9084	0.9847
	GMSD	0.0862	0.0779	0.0886	0.0862	0.0851	0.0258
Boat	PSNR	28.2471	28.7590	28.7991	31.4845	31.6940	36.6481
	SSIM	0.9503	0.9071	0.9248	0.9613	0.9627	0.9818
	GMSD	0.0551	0.0479	0.0641	0.0346	0.0315	0.0095

Table 2 Performance of the different algorithms under 20% noise level

Processed image		ATV	ITV	ITV_Lp	LOGS_Lp	HOGS_Lp	SFT_Lp
Lena512	PSNR	31.7374	31.8185	35.6344	38.8151	39.3321	42.1803
	SSIM	0.9539	0.9556	0.9869	0.9939	0.9944	0.9961
	GMSD	0.0562	0.0545	0.0195	0.0125	0.0108	0.0049
Lena	PSNR	28.4233	28.8501	30.2444	31.2014	31.5262	36.1334
	SSIM	0.7914	0.8770	0.9165	0.9462	0.9494	0.9748
	GMSD	0.0576	0.0498	0.0421	0.0379	0.0346	0.0119
House	PSNR	33.0417	33.8735	34.6895	38.5316	38.8785	42.9098
	SSIM	0.9283	0.9318	0.9060	0.9780	0.9776	0.9836
	GMSD	0.0459	0.0423	0.0395	0.0155	0.0140	0.0054
Gold hill	PSNR	27.5139	27.6994	29.8049	31.3843	31.4681	34.0065
	SSIM	0.8221	0.8347	0.9094	0.9302	0.9308	0.9557
	GMSD	0.0670	0.0722	0.0506	0.0398	0.0344	0.0185
Man	PSNR	27.3771	27.5952	28.6371	29.6909	29.8004	33.8194
	SSIM	0.8054	0.8574	0.8846	0.9267	0.9290	0.9642
	GMSD	0.0625	0.0623	0.0583	0.0435	0.0426	0.0178
Peppers	PSNR	27.6303	28.1957	28.4263	29.4393	29.6445	37.3046
	SSIM	0.8254	0.9300	0.9233	0.9569	0.9507	0.9779
	GMSD	0.0677	0.0531	0.0562	0.0450	0.0448	0.0089
Camera	PSNR	23.5933	23.7337	23.9291	24.5274	24.6687	34.6224
	SSIM	0.6765	0.7819	0.8406	0.8932	0.8940	0.9786
	GMSD	0.0976	0.0861	0.1134	0.0760	0.0750	0.0157
Barbara	PSNR	24.0267	24.0385	24.0870	24.5212	24.7149	31.0463
	SSIM	0.7534	0.7731	0.7756	0.8545	0.8551	0.9646
	GMSD	0.0972	0.0909	0.1058	0.1012	0.1033	0.0354
Boat	PSNR	26.4498	26.6350	26.697	27.6089	28.7908	33.6742
	SSIM	0.7989	0.8162	0.8594	0.9063	0.9165	0.9628
	GMSD	0.0712	0.0687	0.0725	0.0700	0.0468	0.0164

Table 3 Performance of the different algorithms under 30% noise level

Processed image		ATV	ITV	ITV_Lp	LOGS_Lp	HOGS_Lp	SFT_Lp
Lena512	PSNR	30.5510	30.5666	33.7127	36.4906	36.8937	39.1209
	SSIM	0.9403	0.9408	0.9793	0.9890	0.9902	0.9926
	GMSD	0.0705	0.0691	0.0306	0.0203	0.0195	0.0090
Lena	PSNR	27.6453	27.6644	27.6858	29.6372	29.8231	33.3127
	SSIM	0.8423	0.8735	0.8838	0.9259	0.9284	0.9579
	GMSD	0.0749	0.0695	0.0691	0.0469	0.0470	0.0190
House	PSNR	31.5602	30.9632	31.9454	35.9756	36.1164	39.9288
	SSIM	0.8643	0.9070	0.8476	0.9627	0.9628	0.9694
	GMSD	0.0482	0.0511	0.0699	0.0213	0.0210	0.0102
Gold hill	PSNR	24.5521	24.9408	28.1354	29.7735	29.8782	32.1587
	SSIM	0.7011	0.7049	0.8657	0.8901	0.8986	0.9288
	GMSD	0.1160	0.1200	0.0711	0.0538	0.0497	0.0239
Man	PSNR	25.6977	26.1973	26.6629	28.0082	28.2930	31.4129
	SSIM	0.7615	0.7673	0.8089	0.8854	0.8956	0.9400

	GMSD	0.0946	0.0780	0.0909	0.0695	0.0588	0.0265
Peppers	PSNR	26.3440	27.6303	26.7186	27.8560	28.3085	33.4411
	SSIM	0.8796	0.8254	0.8703	0.9113	0.9359	0.9614
	GMSD	0.0917	0.0677	0.8180	0.0592	0.0533	0.0157
Camera	PSNR	21.8731	24.0267	21.9001	23.0165	23.2120	29.9949
	SSIM	0.5683	0.7534	0.7946	0.8419	0.8447	0.9563
	GMSD	0.1454	0.0972	0.1377	0.0978	0.0945	0.0319
Barbara	PSNR	22.8766	24.0267	23.1609	23.0178	23.4166	27.7932
	SSIM	0.7078	0.7534	0.7501	0.7937	0.8103	0.9265
	GMSD	0.1173	0.0972	0.1201	0.1263	0.1177	0.0526
Boat	PSNR	24.9401	26.4498	24.9680	26.4322	26.5506	29.6082
	SSIM	0.7768	0.7989	0.7900	0.8734	0.8769	0.9282
	GMSD	0.0970	0.0712	0.0957	0.0752	0.0758	0.0332

4.3 Comparison with some median filter-based methods

In this section, we compared some median filter-based methods, including median filter method, adaptive switching weight mean filter (ASWMF) [59] method, adaptive frequency median filter (AFMF) [60] method, iterative mean filter (IMF) [61] method, two-stage filter (TSF) [62] method. The experiment results can be found in Table 4-6. As the denoising performance shown in the tables, the proposed model outperforms the median filter-based methods.

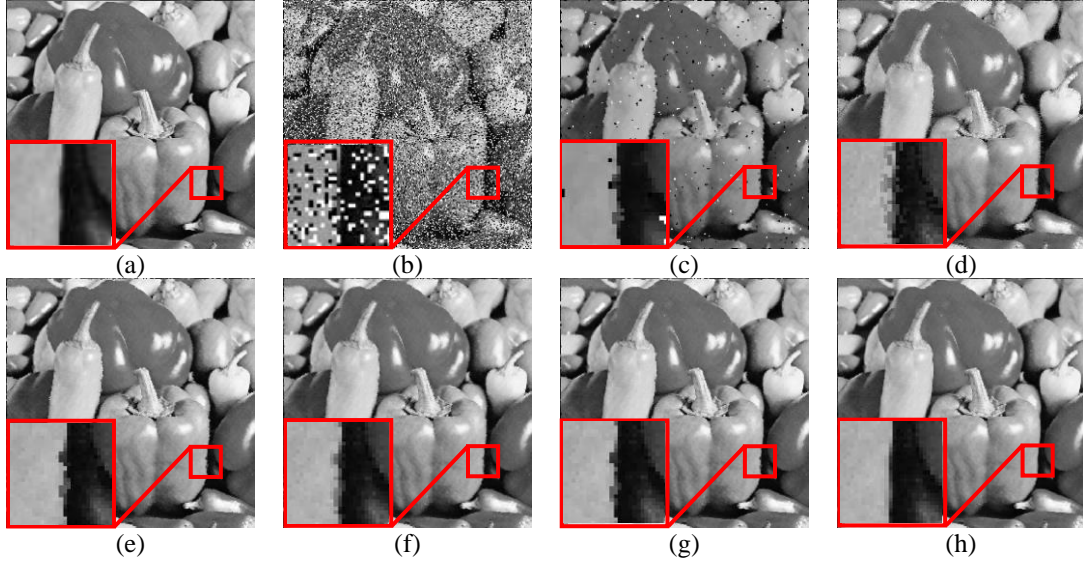


Figure 8 A partial enlarged view of the “Peppers” under 30% salt and pepper noise. (a) Original image of “Peppers”; (b) “Peppers” under 30% noise level interference; (c) MF method; (d) ASWMF method; (e) AFMF method; (f) IMF method; (g) TSF method; (h) proposed method.

To further illustrate the advantage of the proposed model, we shown the enlarged reconstructed image in Figure 8. It is observed in Figure 8 (h) that the Peppers’s edge can be clearly recovered by the proposed method. However, the edges recovered by median filter-based methods were still polluted by the noise. Thus, we can conclude that the proposed method outperforms the compared methods in terms of quantitative and qualitative comparisons.

Table 4 Performance of the different algorithms under 10% noise level

Processed image		MF	ASWMF	AFMF	IMF	TSF	SFT_Lp
Lena512	PSNR	33.0191	37.2039	38.1258	42.3317	43.1522	45.7682
	SSIM	0.9780	0.9948	0.9916	0.9977	0.9977	0.9983

	GMSD	0.0330	0.0106	0.0082	0.0037	0.0036	0.0022
Lena	PSNR	28.4977	34.0741	33.0085	37.1457	38.0998	39.9352
	SSIM	0.8619	0.9719	0.9451	0.9847	0.9865	0.9886
	GMSD	0.0468	0.0155	0.0193	0.0086	0.0097	0.0062
House	PSNR	30.9099	36.0640	36.9043	40.7681	42.5726	46.8257
	SSIM	0.8772	0.9771	0.9464	0.9868	0.9876	0.9928
	GMSD	0.0534	0.0118	0.0122	0.005	0.0043	0.0020
Gold hill	PSNR	27.0210	34.0354	31.0397	36.5352	36.4015	37.6899
	SSIM	0.7664	0.9625	0.9082	0.9777	0.9770	0.9794
	GMSD	0.0623	0.0163	0.0264	0.0103	0.0113	0.0084
Man	PSNR	26.6190	32.7080	30.2940	35.3548	35.8830	39.7596
	SSIM	0.7981	0.9617	0.9140	0.9783	0.9794	0.9818
	GMSD	0.0535	0.0208	0.0303	0.0120	0.0125	0.0104
Peppers	PSNR	29.1800	33.0714	32.2038	36.9602	37.2562	40.6575
	SSIM	0.8832	0.9696	0.9511	0.9868	0.9876	0.9890
	GMSD	0.0378	0.0180	0.0162	0.0071	0.0068	0.0043
Camera	PSNR	26.1096	31.5639	30.2419	31.8594	35.0790	38.3257
	SSIM	0.8629	0.9724	0.9423	0.9796	0.9861	0.9903
	GMSD	0.0616	0.0236	0.0270	0.0167	0.0131	0.0087
Barbara	PSNR	22.4381	31.0825	26.4266	32.4105	31.5581	34.7140
	SSIM	0.7032	0.9638	0.8972	0.9762	0.9726	0.9847
	GMSD	0.0815	0.0289	0.0621	0.0285	0.0316	0.0258
Boat	PSNR	25.0490	31.7254	29.2409	34.1336	34.2986	36.6481
	SSIM	0.7492	0.9599	0.9039	0.9753	0.9747	0.9818
	GMSD	0.0803	0.0219	0.0321	0.0150	0.0175	0.0095

Table 5 Performance of the different algorithms under 20% noise level

Processed image		MF	ASWMF	AFMF	IMF	TSF	SFT_Lp
Lena512	PSNR	28.8822	34.0151	36.7439	39.1499	39.0593	42.1803
	SSIM	0.9345	0.9877	0.9898	0.9949	0.9947	0.9961
	GMSD	0.0805	0.0216	0.0119	0.0077	0.0078	0.0049
Lena	PSNR	25.6222	30.6870	31.9194	34.1172	34.5191	36.1334
	SSIM	0.8129	0.9390	0.9395	0.9682	0.9695	0.9748
	GMSD	0.0901	0.0304	0.0241	0.0166	0.0170	0.0119
House	PSNR	26.7200	33.2079	34.9913	38.0083	37.8885	42.9098
	SSIM	0.8236	0.9539	0.9422	0.9735	0.9720	0.9836
	GMSD	0.1120	0.0232	0.0196	0.0108	0.0095	0.0054
Gold hill	PSNR	24.7292	30.8423	30.1820	33.1605	32.9473	34.0065
	SSIM	0.7163	0.9223	0.9002	0.9509	0.9494	0.9557
	GMSD	0.0965	0.0285	0.0333	0.0216	0.0214	0.0185
Man	PSNR	24.4622	29.7477	29.5505	32.1808	32.5296	33.8194
	SSIM	0.7477	0.9220	0.9074	0.9533	0.9559	0.9642
	GMSD	0.0890	0.0328	0.0347	0.0223	0.0200	0.0178
Peppers	PSNR	25.8728	29.8470	30.6801	33.8627	34.4772	37.3046
	SSIM	0.8339	0.9400	0.9442	0.9714	0.9724	0.9779
	GMSD	0.0783	0.0308	0.0242	0.0131	0.0139	0.0089

Camera	PSNR	23.9891	28.5273	29.0985	31.6309	31.7084	34.6224
	SSIM	0.8156	0.9415	0.9364	0.9695	0.9692	0.9786
	GMSD	0.1121	0.0388	0.0326	0.0242	0.0234	0.0157
Barbara	PSNR	21.3825	28.1177	25.9710	29.1070	28.1235	31.0463
	SSIM	0.6708	0.9248	0.8885	0.9469	0.9387	0.9646
	GMSD	0.1151	0.0435	0.0714	0.0456	0.0564	0.0354
Boat	PSNR	23.2736	28.9017	28.3783	31.1735	30.9221	33.6742
	SSIM	0.7003	0.9204	0.8950	0.9493	0.9449	0.9628
	GMSD	0.1063	0.0380	0.0384	0.0251	0.0275	0.0164

Table 6 Performance of the different algorithms under 30% noise level

Processed image		MF	ASWMF	AFMF	IMF	TSF	SFT_Lp
Lena512	PSNR	23.4716	32.1691	35.3407	36.9242	36.6563	39.1209
	SSIM	0.7748	0.9782	0.9870	0.9910	0.9906	0.9926
	GMSD	0.1726	0.0335	0.0154	0.0134	0.0133	0.0090
Lena	PSNR	21.7882	28.7916	30.5818	32.2336	36.6276	33.3127
	SSIM	0.6694	0.9042	0.9254	0.9511	0.9906	0.9579
	GMSD	0.1628	0.0458	0.0292	0.0248	0.0134	0.0190
House	PSNR	22.8304	31.0455	33.5705	35.7666	35.1875	39.9288
	SSIM	0.6867	0.9242	0.9325	0.9579	0.9542	0.9694
	GMSD	0.1979	0.0390	0.0215	0.0165	0.0162	0.0102
Gold hill	PSNR	21.6025	28.9334	29.2643	31.0936	30.9446	32.1587
	SSIM	0.6142	0.8779	0.8809	0.9216	0.9176	0.9288
	GMSD	0.1514	0.0415	0.0374	0.0288	0.0323	0.0239
Man	PSNR	21.4300	27.9398	28.5007	30.4007	30.3540	31.4129
	SSIM	0.6309	0.8786	0.8923	0.9285	0.9284	0.9400
	GMSD	0.1435	0.0492	0.0422	0.0337	0.0306	0.0265
Peppers	PSNR	22.2545	27.9049	28.8770	31.5784	31.9965	33.4411
	SSIM	0.7104	0.9058	0.9342	0.9557	0.9552	0.9614
	GMSD	0.1431	0.0455	0.0298	0.0237	0.0191	0.0157
Camera	PSNR	20.8895	26.6380	27.7981	29.6247	29.4920	29.9949
	SSIM	0.6769	0.9071	0.9264	0.9505	0.9498	0.9563
	GMSD	0.1998	0.0565	0.0439	0.0344	0.0341	0.0319
Barbara	PSNR	19.4435	24.1493	25.0142	27.3986	26.3904	27.7932
	SSIM	0.5681	0.8789	0.8667	0.9184	0.9063	0.9265
	GMSD	0.1673	0.0629	0.0821	0.0575	0.0711	0.0526
Boat	PSNR	21.0431	26.9928	27.4286	29.0716	28.8486	29.6082
	SSIM	0.6078	0.8775	0.8799	0.9186	0.9141	0.9282
	GMSD	0.1544	0.0513	0.0456	0.0364	0.0394	0.0332

4.4 Ablation experiments

To further evaluate the key parts of the proposed model, we performed ablation experiments for the MCA, mask matrix, sparse transform, and l_p quasi-norm.

4.4.1 Ablation of the MCA

We compared the proposed model with the sparse representation-based denoising model (the objective function is $F = \underset{F}{\operatorname{argmin}} \alpha_0 \|\mathbf{M} \circ (\mathbf{F}) - \mathbf{G}\|_{p_0}^{p_0} + \alpha_1 \|\mathbf{D}(\mathbf{F})\|_{p_1}^{p_1}$), in which the recovery image is not

considered as the sum of the cartoon and texture parts. Although the reconstructed qualities of the cartoon part shown in Figure 9 (c) and the texture part shown in Figure 9 (d) are less than those of the sparse representation-based model, the final reconstructed image is better than the recovery image of the sparse representation-based model. The PSNR obtained by the proposed model is 0.4972 dB higher than that obtained by the sparse representation-based model. This is because the MCA framework restores the image hierarchically. In this way, the low-frequency component (in the cartoon part) and the high-frequency component (in the texture part) do not interfere with each other to obtain a more detailed restored image.



(a)



(b)



(c)



(d)



(e)

Figure 9 Results of the ablation experiments. (a) “Lena512” under 20% salt and pepper noise (PSNR=12.4361, SSIM=0.2687, GMSD= 0.2947); (b) reconstructed image (PSNR=41.6831, SSIM=0.9958, GMSD= 0.0055) by the objective function $F = \underset{F}{\operatorname{argmin}} \alpha_0 \|\mathbf{M} \circ (\mathbf{F}) - \mathbf{G}\|_{p_0}^{p_0} + \alpha_1 \|\mathbf{D}(\mathbf{F})\|_{p_1}^{p_1}$; (c) reconstructed cartoon part (PSNR=38.3801, SSIM=0.9892, GMSD=0.0127) by the proposed model; (d) reconstructed texture part (PSNR=5.6703, SSIM=1.8204E-4, GMSD= 0.3186) by the proposed model; (e) reconstructed image (PSNR= **42.1803**, SSIM= **0.9961**, GMSD=**0.0049**) by the proposed model.

4.4.2 Ablation of the mask matrix

In this section, we describe the effects of the mask matrix \mathbf{M} in the proposed model. Based on the test image shown in Figure 6 (a), Figure 10 shows the result obtained by the objective function without the mask matrix (the objective function is $[\mathbf{F}_T, \mathbf{F}_C] = \underset{[\mathbf{F}_T, \mathbf{F}_C]}{\operatorname{argmin}} \alpha_0 \|\mathbf{F}_T + \mathbf{F}_C - \mathbf{G}\|_{p_0}^{p_0} + \alpha_1 \|\mathbf{D}(\mathbf{F}_C)\|_{p_1}^{p_1} + \alpha_2 \|\mathbf{D}(\mathbf{F}_T)\|_{p_2}^{p_2}$) and the result obtained by the proposed model.

As shown in Figure 10, the quality of the reconstructed model without the mask matrix is considerably reduced. The main reason for this phenomenon is that the mask matrix contains the noise position information, which plays a role in protecting the area not polluted by noise. In this way, the clean data are protected. In addition, the area polluted by noise can be sparsely represented by the Framelet coefficients. Thus, the mask matrix is significant for preserving the image details.



Figure 10 Results of the ablation experiments. (a) The reconstructed image (PSNR= 34.9018, SSIM=0.9866, GMSD= 0.0194) by the objective function

$$[\mathbf{F}_T, \mathbf{F}_C] = \underset{[\mathbf{F}_T, \mathbf{F}_C]}{\operatorname{argmin}} \alpha_0 \|\mathbf{F}_T + \mathbf{F}_C - \mathbf{G}\|_{p_0}^{p_0} + \alpha_1 \|\mathbf{D}(\mathbf{F}_C)\|_{p_1}^{p_1} + \alpha_2 \|\mathbf{D}(\mathbf{F}_T)\|_{p_2}^{p_2};$$

(b) the reconstructed image (PSNR= 42.1803, SSIM=0.9961, GMSD= 0.0049) by the proposed model.

4.4.3 Ablation of the sparse transform

We compared the wavelet-based model (the objective function is $[\mathbf{F}_T, \mathbf{F}_C] = \underset{[\mathbf{F}_T, \mathbf{F}_C]}{\operatorname{argmin}} \alpha_0 \|\mathbf{M} \circ (\mathbf{F}_T + \mathbf{F}_C) - \mathbf{G}\|_{p_0}^{p_0} + \alpha_1 \|\mathbf{W}(\mathbf{F}_C)\|_{p_1}^{p_1} + \alpha_2 \|\mathbf{W}(\mathbf{F}_T)\|_{p_2}^{p_2}$) and the proposed model. The wavelet basis is the Haar wavelet [63]. The WT and inverse WT were implemented using the Mallat algorithm [64]. The results of the ablation experiment are shown in Figure 10.



Figure 11 Results of the ablation experiments. (a) The reconstructed image (PSNR=33.1442, SSIM=0.9623, GMSD=0.0278) by the objective function

$$[\mathbf{F}_T, \mathbf{F}_C] = \underset{[\mathbf{F}_T, \mathbf{F}_C]}{\operatorname{argmin}} \alpha_0 \|\mathbf{M} \circ (\mathbf{F}_T + \mathbf{F}_C) - \mathbf{G}\|_{p_0}^{p_0} + \alpha_1 \|\mathbf{W}(\mathbf{F}_C)\|_{p_1}^{p_1} + \alpha_2 \|\mathbf{W}(\mathbf{F}_T)\|_{p_2}^{p_2};$$

(b) the reconstructed image (PSNR=42.1803, SSIM=0.9961, GMSD=0.0049) by the proposed model.

As shown in Figure 11, the image quality restored using the Haar WT is not as high as that restored

by the SFT. Because the SFT does not have the down-sample operation in the WT, the Framelet coefficients do not need to be up-sampled by padding zeros when reconstructing the image; this avoids the image information loss in the WT and inverse WT. In addition, compared with the traditional wavelet transform, SFT adds a high-pass filter, which is capable of decomposing the image texture information more accurately than the WT. Therefore, the quality of the recovery image obtained via SFT was higher than that of the WT.

4.4.4 Ablation of the l_p quasi-norm

We compared the proposed model with the model using the l_1 norm (the objective function is $[F_T, F_C] = \underset{[F_T, F_C]}{\operatorname{argmin}} \alpha_0 \|M \circ (F_T + F_C) - G\|_1 + \alpha_1 \|D(F_C)\|_1 + \alpha_2 \|D(F_T)\|_1$). The results of the ablation experiment are shown in Figure 12. The PSNR obtained by the proposed model was 0.5848 higher than that obtained by the model with the l_1 norm.



Figure 12 Results of the ablation experiments. (a) The reconstructed image (PSNR=41.5955, SSIM=0.9957, GMSD=0.0054) by the objective function

$[F_T, F_C] = \underset{[F_T, F_C]}{\operatorname{argmin}} \alpha_0 \|M \circ (F_T + F_C) - G\|_1 + \alpha_1 \|D(F_C)\|_1 + \alpha_2 \|D(F_T)\|_1$; (b) the reconstructed image (PSNR=42.1803, SSIM=0.9961, GMSD=0.0049) by the proposed model.

Because the l_p quasi-norm can express the sparsity more accurately than the l_1 norm, the model with the l_p quasi-norm achieves a better reconstructed result. Moreover, the l_p quasi-norm has more flexible degrees of freedom and can be adjusted with the change in noise level to obtain the best image restoration effect. Therefore, the proposed model has a better model expression ability and better image restoration effect.

5. Conclusion

In this paper, we propose a salt and pepper noise removal method based on MCA with the l_p quasi-norm. In the proposed method, we first explore the noise position information by capturing the amplitude characteristics of salt and pepper noise to determine the mask matrix. By introducing the mask matrix and the SFT into the MCA framework, the image is decomposed into cartoon and texture parts. The l_p quasi-norm is adopted to depict the sparsity of salt and pepper noise and the Framelet coefficients. Several experiments were conducted to verify the effectiveness of the proposed model. The main findings of this study are summarized as follows:

(1) Under different levels of noise in the test image, the PSNR, SSIM, and GMSD of the recovery images obtained by the proposed model are better than those of the other denoising methods, demonstrating that the denoising effect of the proposed model is excellent.

(2) The dynamic iteration curves showed that the proposed method can obtain a convergent solution in relatively fewer steps.

(3) Ablation experiments showed that the key components (MCA framework, mask matrix, SFT, and l_p quasi-norm) of the proposed model are significant in determining the image denoising performance.

However, the proposed model also has some limitations. The main limitation is that the parameter selection is adjusted manually. In addition, the computational efficiency of the model is low. Thus, we will focus on solving the limitations in further study.

Acknowledgements

This work is supported by natural science foundation project of Fujian Province (2020J05169, 2020J01816); principal foundation of Minnan Normal University (KJ19019); young and middle-aged teachers research and education project of education department in Fujian Province (JAT190393, JAT190382); high-level science research project of Minnan Normal University (GJ19019).

Reference

- [1] M. Yildirim, Analog circuit implementation based on median filter for salt and pepper noise reduction in image, *Analog Integrated Circuits and Signal Processing*, 107 (2021) 195-202.
- [2] S. Rahimi, A. Aghagolzadeh, H. Seyedarabi, Human detection and tracking using new features combination in particle filter framework, *Machine Vision and Image Processing*, 72 (2013) 349-354.
- [3] Y.-Y. Liu, X.-L. Zhao, Y.-B. Zheng, T.-H. Ma, H. Zhang, Hyperspectral image restoration by tensor fibered rank constrained optimization and plug-and-play regularization, *IEEE Transactions on Geoscience and Remote Sensing*, (2021).
- [4] J.-H. Yang, X.-L. Zhao, T.-Y. Ji, T.-H. Ma, T.-Z. Huang, Low-rank tensor train for tensor robust principal component analysis, *Applied Mathematics and Computation*, 367 (2020) 124783.
- [5] K.H. Jin, J.C. Ye, Sparse and low-rank decomposition of a Hankel structured matrix for impulse noise removal, *IEEE Transactions on Image Processing*, 27 (2017) 1448-1461.
- [6] S. Vijayan, A. Chilambuchelvan, G. Balasubramanian, Gowrison, Probabilistic decision based filter to remove impulse noise using patch else trimmed median, *AEUE - International Journal of Electronics and Communications*, 70 (2016) 471-481.
- [7] M. González-Hidalgo, S. Massanet, A. Mir, D. Ruiz-Aguilera, Impulsive noise removal with an adaptive weighted arithmetic mean operator for any noise density, *Applied Sciences*, 11 (2021) 560.
- [8] A. Shaveta, H. Madasu, G. Gaurav, Filtering impulse noise in medical images using information sets, *Pattern Recognition Letters*, 139 (2018) 1-9.
- [9] H. Hwang, R.A. Haddad, Adaptive median filters: new algorithms and results, *IEEE Transactions on Image Processing*, 4 (1995) 499-502.
- [10] R.H. Chan, C.-W. Ho, M. Nikolova, Salt-and-pepper noise removal by median-type noise detectors and detail-preserving regularization, *IEEE Transactions on Image Processing*, 14 (2005) 1479-1485.
- [11] Y. Dong, S. Xu, A new directional weighted median filter for removal of random-valued impulse noise, *IEEE Signal Processing Letters*, 14 (2007) 193-196.
- [12] S. Li, Y. He, Y. Chen, W. Liu, Y. Xi, Z. Peng, Fast multi-trace impedance inversion using anisotropic total p-variation regularization in the frequency domain, *Journal of Geophysics and Engineering*, 15 (2018) 2171-2182.
- [13] H. Wu, Y.M. He, Y.P. Chen, S. Li, Z. Peng, Seismic acoustic impedance inversion using mixed

- second-order fractional ATpV regularization, *IEEE Access*, 8 (2019) 3442-3452.
- [14] S. Osher, M. Burger, D. Goldfarb, J. Xu, W. Yin, An iterative regularization method for total variation-based image restoration, *SIAM Journal on Multiscale Modeling & Simulation*, 4 (2005) 460-489.
- [15] L. Wang, Y. Chen, F. Lin, Y. Chen, F. Yu, Z. Cai, Impulse noise denoising using total variation with overlapping group sparsity and Lp-pseudo-norm shrinkage, *Applied Sciences*, 8 (2018) 2317.
- [16] Y. Shi, Q. Chang, Efficient algorithm for isotropic and anisotropic total variation deblurring and denoising, *Journal of Applied Mathematics*, 2013 (2013) 1-15.
- [17] L.I. Rudin, S. Osher, E. Fatemi, Nonlinear total variation based noise removal algorithms, *Physica D: Nonlinear Phenomena*, 60 (1992) 259-268.
- [18] Y. Jin, L. Yu, G. Li, S. Fei, A 6-DOFs event-based camera relocalization system by CNN-LSTM and image denoising, *Expert Systems with Applications*, 170 (2020) 389-393.
- [19] K. Zhang, W. Zuo, L. Zhang, FFDNet: Toward a fast and flexible solution for CNN based image denoising, *IEEE Transactions on Image Processing*, 27 (2017) 4608-4622.
- [20] Y. Xing, J. Xu, J. Tan, D. Li, W. Zha, Deep CNN for removal of salt and pepper noise, *Image Processing, The Institution of Engineering and Technology*, 13 (2019) 1550-1560.
- [21] B. Fu, X. Zhao, Y. Li, X. Wang, Y. Ren, A convolutional neural networks denoising approach for salt and pepper noise, *Multimedia Tools and Applications*, 78 (2018) 30707-30721.
- [22] G. Li, X. Xu, M. Zhang, Q. Liu, Densely connected network for impulse noise removal, *Pattern Analysis and Applications*, 23 (2020) 1263-1275.
- [23] C.T. Lu, H.J. Hsu, L.L. Wang, Image denoising using DLNN to recognize the direction of pixel variation, *Signal Image and Video Processing*, (2021) 1-10.
- [24] R. Abiko, M. Ikehara, Blind denoising of mixed Gaussian-impulse noise by single CNN, in: *ICASSP 2019-2019 IEEE International Conference on Acoustics, Speech and Signal Processing (ICASSP)*, IEEE, 2019, pp. 1717-1721.
- [25] Y.-T. Wang, X.-L. Zhao, T.-X. Jiang, L.-J. Deng, Y. Chang, T.-Z. Huang, Rain streaks removal for single image via Kernel-guided convolutional neural network, *IEEE Transactions on Neural Networks and Learning Systems*, (2020).
- [26] X.-L. Zhao, W.-H. Xu, T.-X. Jiang, Y. Wang, M.K. Ng, Deep plug-and-play prior for low-rank tensor completion, *Neurocomputing*, 400 (2020) 137-149.
- [27] A. Bijalwan, A. Goyal, N. Sethi, Wavelet transform based image denoise using threshold approaches, *International Journal of Engineering & Advanced Technology*, 2012 (2012) 218-221.
- [28] X. Li, Y.S. He, X. Zhan, The optimization research of geo-environmental monitoring image fusion based on framelet, *Advanced Materials Research*, 2012 (2010) 218-221.
- [29] H. Wu, Z. Liang, G. Gu, H. Tao, Q. Ning, Color image enhancement based on LLL tricolor image denoising and fusion, *Journal of Applied Optics*, 39 (2018) 59-63.
- [30] Z. Cheng, Y. Chen, L. Wang, F. Lin, H. Wang, Y. Chen, Four-directional total variation denoising using fast fourier transform and ADMM, in: *International Conference on Image, Vision and Computing*, New York: Institute of Electrical and Electronics Engineers, 2018, pp. 379-383.
- [31] X. Wang, R.S. Istepanian, Y.H. Song, Microarray image enhancement by denoising using stationary wavelet transform, *IEEE Transactions on Nanobioscience*, 2 (2003) 184-189.
- [32] S. Yan, X. Yang, Y. Guo, H., Translation invariant directional framelet transform combined with gGabor filters for image denoising, *IEEE Transactions on Image Processing*, 23 (2013) 44-55.
- [33] B. Han, Properties of discrete framelet transforms, *Mathematical Modelling of Natural Phenomena*,

8 (2013) 18-47.

[34] J. Liu, Y. Lou, G. Ni, T. Zeng, An image sharpening operator combined with framelet for image deblurring, *Inverse Problems*, 36 (2020) 045015.

[35] C. Zeng, C. Wu, R. Jia, Non-Lipschitz models for image restoration with impulse noise removal, *SIAM Journal on Imaging Sciences*, 12 (2019) 420-458.

[36] Y.P. Chen, Z.M. Peng, A. Gholami, J.W. Yan, S. Li, Seismic signal sparse time-frequency representation by L_p -quasinorm constraint, *Digital Signal Processing*, 87 (2019) 34-42.

[37] J. Yang, Y. Chen, Z. Chen, Infrared image deblurring via high-order total variation and L_p -pseudonorm shrinkage, *Applied Sciences*, 10 (2020) 2533.

[38] X.G. Liu, Y.P. Chen, Z.M. Peng, J. Wu, Total variation with overlapping group sparsity and L_p quasinorm for infrared image deblurring under salt-and-pepper noise, *Journal of Electronic Imaging*, 28 (2019) 1.

[39] F. Lin, Y. Chen, L. Wang, Y. Chen, W. Zhu, F. Yu, An efficient image reconstruction framework using total variation regularization with L_p -quasinorm and group gradient sparsity, *Information*, 10 (2019) 115.

[40] F. Lin, Y. Chen, Y. Chen, F. Yu, Image deblurring under impulse noise via total generalized variation and non-convex shrinkage, *Algorithms*, 12 (2019) 221.

[41] R. Chartrand, Shrinkage mappings and their induced penalty functions, in: 2014 IEEE International Conference on Acoustics, Speech and Signal Processing (ICASSP), IEEE, 2014, pp. 1026-1029.

[42] N. Sprljan, E. Izquierdo, New perspectives on image compression using a cartoon - texture decomposition model, in: *Video/image Processing & Multimedia Communications, Eurasp Conference Focused on*, 2003, pp. 359-368.

[43] J. Bobin, J.L. Starck, J.M. Fadili, Y. Moudden, D.L. Donoho, Morphological component analysis : an adaptive thresholding strategy, in: J. Bobin, J.L. Starck, J.M. Fadili, Y. Moudden, D.L. Donoho (Eds.) *The Institute of Electrical and Electronics Engineers Transactions on Image Processing*, 2007, pp. 2675-2681.

[44] M. Elad, J.L. Starck, P. Querre, Simultaneous cartoon and texture image inpainting using morphological component analysis, *Applied & Computational Harmonic Analysis*, 19 (2005) 340-358.

[45] J.M. Fadili, J.L. Starck, M. Elad, D.L. Donoho, MCALab: reproducible research in signal and image decomposition and inpainting, *Computing in Science & Engineering*, 12 (2010) 44-63.

[46] J.L. Starck, M. Elad, D. Donoho, Redundant multiscale transforms and their application for morphological component separation, *Advances in Imaging & Electron Physics*, 132 (2004) 287-348.

[47] H. Chen, S., Z. Xu, H., Q. Feng, S., Y. Fan, Y., Z. Li, H., An L_0 regularized cartoon-texture decomposition model for restoring images corrupted by blur and impulse noise, *Signal Processing: Image Communication*, 82 (2020) 115762.

[48] H. Chen, S., Y. Fan, Y., Q. Wang, H., Z. Li, H., Morphological component image restoration by employing bregmanized sparse regularization and anisotropic total variation, *Circuits Systems and Signal Processing*, 39 (2020) 2507-2532.

[49] S. Boyd, N. Parikh, E.C. hu, B. Peleato, E.K. J, Distributed optimization and statistical learning via the alternating direction method of multipliers, *Foundations & Trends in Machine Learning*, 3 (2010) 1-122.

[50] M. Hong, Z.-Q. Luo, On the linear convergence of the alternating direction method of multipliers, *Mathematical Programming*, 162 (2017) 165-199.

- [51] Z. Wang, A.C. Bovik, H.R. Sheikh, E.P. Simoncelli, Image quality assessment : From error visibility to structural similarity, *IEEE Transactions on Image Processing*, 13 (2004) 600-612.
- [52] R. Chartrand, Shrinkage mappings and their induced penalty functions, in: *IEEE International Conference on Acoustics, Speech and Signal Processing*, 2014, pp. 1026-1029.
- [53] G.P. Nason, B.W. Silverman, The stationary wavelet transform and some statistical applications, in: *Wavelets and statistics*, Springer, 1995, pp. 281-299.
- [54] H. Al-Taai, A novel fast computing method for framelet coefficients, *American Journal of Applied Sciences*, 5 (2008) 1522-1527.
- [55] Eisenstat, C. Stanley, Efficient implementation of a class of preconditioned conjugate gradient methods, *SIAM Journal on Scientific & Statistical Computing*, 2 (1981) 1-4.
- [56] W. Xue, L. Zhang, X. Mou, A.C. Bovik, Gradient magnitude similarity deviation: A highly efficient perceptual image quality index, *IEEE Transactions on Image Processing*, 23 (2013) 684-695.
- [57] V. Vishnevskiy, T. Gass, G. Szekely, C. Tanner, O. Goksel, Isotropic total variation regularization of displacements in parametric image registration, *IEEE Transactions on Medical Imaging*, 36 (2016) 385-395.
- [58] H. Wu, S. Li, Y. Chen, Z. Peng, Seismic impedance inversion using second-order overlapping group sparsity with A-ADMM, *Journal of Geophysics and Engineering*, 17 (2020) 97-116.
- [59] D.N. Thanh, N.N. Hien, P. Kalavathi, V.S. Prasath, Adaptive switching weight mean filter for salt and pepper image denoising, *Procedia Computer Science*, 171 (2020) 292-301.
- [60] U. Erkan, S. Enginoğlu, D.N. Thanh, L.M. Hieu, Adaptive frequency median filter for the salt and pepper denoising problem, *IET Image Processing*, 14 (2020) 1291-1302.
- [61] D.N.H. Thanh, S. Enginoğlu, An iterative mean filter for image denoising, *IEEE Access*, 7 (2019) 167847-167859.
- [62] D.N. Thanh, N.H. Hai, V.S. Prasath, J.M.R. Tavares, A two-stage filter for high density salt and pepper denoising, *Multimedia Tools and Applications*, 79 (2020) 21013-21035.
- [63] R.S. Stanković, B.J. Falkowski, The Haar wavelet transform: its status and achievements, *Computers & Electrical Engineering*, 29 (2003) 25-44.
- [64] S.G. Mallat, A theory for multiresolution signal decomposition: the wavelet representation, *IEEE Transactions on Pattern Analysis and Machine Intelligence*, 11 (1989) 674-693.